SPECIAL IFloodS COLLECTION

Overview of the D3R Observations during the IFloodS Field Experiment with Emphasis on Rainfall Mapping and Microphysics

ROBERT M. BEAUCHAMP, V. CHANDRASEKAR, AND HAONAN CHEN

Colorado State University, Fort Collins, Colorado

MANUEL VEGA

NASA Goddard Space Flight Center, Greenbelt, Maryland, and Colorado State University, Fort Collins, Colorado

(Manuscript received 2 February 2015, in final form 5 June 2015)

ABSTRACT

The NASA dual-frequency, dual-polarization Doppler radar (D3R) was deployed as part of the GPM Iowa Flood Studies (IFloodS) ground validation field campaign from 1 May through 15 June 2013. The D3R participated in a multi-instrument targeted investigation of convective initiation and hydrological response in the midwestern United States. An overview of the D3R's calibration and observations is presented. A method for attenuation correction of Ka-band observations using Ku-band results is introduced. Dual-frequency ratio estimates in stratiform rain and ice are presented and compared with theoretical values. Ku-band quantitative precipitation estimation results are validated against IFloodS ground instruments.

1. Introduction

The NASA dual-frequency, dual-polarization Doppler radar (D3R) is a deployable weather radar that enables synchronized, beam-aligned observations at Ku (13.91 GHz) and Ka band (35.56 GHz; Vega et al. 2014). The D3R was designed as a ground-based radar with operating frequencies analogous to the Global Precipitation Measurement (GPM) core satellite Dual-Frequency Precipitation Radar (DPR). As part of the ground validation mission for the GPM program, the D3R is a critical platform for comparison with the DPR because of its similar operational frequency and the ability to be deployed for targeted, long-term observation of meteorological events. The D3R provides high-temporal-resolution and high-spatial-resolution observations for a more detailed understanding of precipitation that will ultimately be used to refine algorithms for retrieval of microphysical properties (Vega et al. 2014).

The D3R is equipped with a solid-state transmitter system and coaligned, beam-matched antennas. The D3R allows for simultaneous dual-polarization observation of the same volume at two frequencies. The Ku band provides greater penetration into moderate and heavy convection. The Ka band has enhanced sensitivity to light rain and snow but is more susceptible to attenuation in moderate and heavy precipitation. The solid-state transmitter and receiver design supports reconfigurable transmitter waveforms and receiver filters, making the D3R an agile research platform for microphysical investigation.

The D3R was deployed collocated with NASA's S-band polarimetric radar (NPOL) during the NASA Iowa Flood Studies (IFloodS) field campaign as part of the GPM ground validation. Both D3R and NPOL were deployed in Traer, Iowa, from 1 May to 15 June 2013 to observe precipitation in concert with an array of ground instruments, NEXRAD S-band radars, and the University of Iowa's X-band radars in the area of the Cedar River and Iowa River basins. During the field campaign, severe flooding was observed in the surrounding areas and river basins. April and May of 2013 were the wettest on record, with the area experiencing unprecedented rainfall for the 2013 spring season in its 141 years of record (as of 2013; Hillaker 2013). The dataset collected by D3R and other instrumentation deployed for the

Corresponding author address: V. Chandrasekar, Colorado State University, 1373 Campus Delivery, Fort Collins, CO 80523.
E-mail: chandra@engr.colostate.edu

DOI: 10.1175/JHM-D-15-0023.1

© 2015 American Meteorological Society

IFloodS field experiment is, in part, being used to better understand and model the microphysical structure of precipitation and the hydrological response of the IFloodS region.

The IFloodS field campaign was the second operational D3R deployment and the first summer deployment of the D3R, demonstrating continuous operation in warm, humid conditions. The IFloodS experiment represents another milestone D3R event as it was the first deployment of the high-powered (40 W) Ka-band transmitter that replaced the temporary 1 W stand-in. The D3R operated continuously during the campaign, experiencing only one non-radar-related issue. This deployment demonstrated the D3R's robustness and completed the operational validation of the radar over its anticipated operating temperature range [supplementing validation during winter operations in early 2012 as part of the NASA GPM Cold-Season Precipitation Experiment (GCPEx)]. The high-powered Ka-band solid-state transmitter was successfully demonstrated. The upgrade provides a 16-dB improvement in sensitivity compared to the 1 W transmitter. The upgrade increases the effective operational range of the Ka band and enhances the capability of the D3R for microphysical studies.

The D3R Ku-band radar's rainfall mapping capability, also referred to as quantitative precipitation estimation (QPE), is examined. The IFloodS field campaign provides an ideal test bed for observation and cross validation with ground instruments. For comparison between ground instruments and the D3R observations, Autonomous Parsivel Unit (APU) disdrometers and rain gauges (Tokay et al. 2014) are considered here. For accurate microphysical investigation of hydrometeors, it is necessary to ensure that the radar estimates are well calibrated and corrected for attenuation effects. The D3R calibration results and preliminary attenuation-correction method for IFloodS are examined in section 3. The cross-validation results using dual-frequency observations and the other instruments deployed at IFloodS are compared in section 4. Quantitative precipitation estimates based on specific differential phase K_{dp} using Ku-band observations are presented in section 5. Finally, section 6 summarizes the D3R's performance and results from the IFloodS ground validation field experiment.

2. D3R overview at IFloodS

During the field experiment, D3R collected over 45 000 scans in coordination with NPOL and the other deployed ground instruments as part of the IFloodS field campaign. There were observations of precipitation on 36 of the 46 days during the experiment. From these, there are no less than five severe convective thunderstorms, two squall lines, and four stratiform rain cases. Table 1 provides a qualitative summary of the D3R observations during the deployment.

The D3R was able to observe, unobstructed, from 90° clockwise to 230° in azimuth and from 0° to 90° in elevation. Observations were made along a line of ground instruments to the southeast that included an array of disdrometers and rain gauges. The D3R's maximum range of 39.75 km allowed coordinated observations with a multitude of instrument types: the NPOL, four APUs, two rain gauges, and three 2D video disdrometers (2DVDs). The ground instruments mentioned were deployed along a radial at approximately 130.4° in azimuth from the radar site. This radial was selected for coordinated RHI scans between D3R and NPOL to maximize the opportunity for cross validation and microphysical investigation using the diverse array of instruments. A map of the location of D3R, NPOL, and the ground instruments discussed here is shown in Fig. 1. The geographic coordinates and the relative bearing and range from the D3R to the ground instruments are presented in Table 2.

3. D3R system calibration and attenuation correction

The calibration of radar systems, such as the D3R, is necessary for accurate retrievals (Vega et al. 2014). A variety of calibration methods are considered to provide consistent and redundant verification of the radar system parameters necessary for accurate and precise radar observations. These system parameters include transmitted power, receiver gain, antenna pointing angle, and antenna coalignment. The time scales in which the various calibration techniques are used depend on the rate of variation and the ability to track parameter drift during normal operation. The results specific to D3R's deployment and operation in IFloodS are discussed, with a focus on demonstrating the accuracy of D3R's meteorological parameter estimation.

a. System calibration

A full system characterization of the radar was performed using calibrated test equipment. This procedure is invasive and required breaking connections at reference planes in the radar system for injection and measurement of signals. Because of the complexity and invasive nature of this characterization, it is generally only performed during scheduled maintenance or when radar component changes occur (component changes may have slight performance deviations from unit to unit). The signal paths, for injection or monitoring, are

TABLE 1. Summary of D3R observations (by date) during the IFloodS field campaign.

Date	Summary
9 May 2013	Stratiform and isolated weak convection
10 May 2013	Stratiform and isolated weak convection
15 May 2013	Squall line
19 May 2013	Large convection with convective stratiform
20 May 2013	Convection and convective stratiform
21 May 2013	Convection and convective stratiform
22 May 2013	Light (<20 dBZ) widespread and isolated stratiform
23 May 2013	Light (<20 dBZ) widespread and isolated stratiform
25 May 2013	Heavy stratiform
26 May 2013	Mild convection and heavy stratiform
27 May 2013	Light widespread stratiform
28 May 2013	Scattered convection embedded in stratiform
29 May 2013	Heavy convection
30 May 2013	Convection and stratiform
1 Jun 2013	Very light stratiform (<15 dBZ), scattered heavy stratiform
2 Jun 2013	Squall line
4 Jun 2013	Convection and heavy stratiform
5 Jun 2013	Convection and heavy stratiform
6 Jun 2013	Sparse convection
7 Jun 2013	Sparse convection
8 Jun 2013	Brief widespread stratiform
9 Jun 2013	Widespread light stratiform and linear MCS
10 Jun 2013	Linear MCS
12 Jun 2013	Large convective outflow plume and heavy stratiform

broken at specific calibration planes, which allows for deterministic characterization of system performance between fixed points. After initial characterization is performed using the test equipment, the internal calibration hardware may be used to track slight variations in the system's performance. The radar's receiver provides a consistent monitor of the radar's performance to estimate any parameter change in the transmitter and receiver paths from the calibration planes.

A metallic sphere is used as an overall, end-to-end radar system calibration target. The metal sphere provides a known radar cross section. The metal sphere is tethered to a balloon and released on a free-flight trajectory while being tracked and observed by the radar. The radar observations are compared against the expected radar cross section for valid observations. Deviation of the observations from the theoretical curve provides an overall radar calibration taking into account all components. Calibration of reflectivity Z with less than 1 dB absolute error is expected using this method. For the IFloodS experiment, a sphere calibration was performed using a 254-mm (10 in.) diameter metal sphere starting at 0000 UTC 14 June 2013. The sphere calibration was performed on a clear, dry, calm evening, and the sphere flight path was well clear of the sun. The sphere calibration results, in Fig. 2, show that the radar's horizontal polarization reflectivity calibration Z_h error is less than 0.5 dB for both frequencies.

For D3R, solar scans are performed primarily as a means of verifying antenna absolute alignment and coalignment of the Ku- and Ka-band antennas. The relative position of the solar radiation compared to the expected position of the sun is compared. When the centroid of the relative position is zero, the antenna positioner's absolute calibration is perfect. Using the same technique, the antenna coalignment is verified with results presented in Fig. 3. For the IFloodS campaign, the coalignment is 0.01° in azimuth and 0.11° in elevation with an absolute alignment error less than 0.06° in azimuth and 0.15° in elevation. A more detailed discussion of the D3R antenna coalignment can be found in Vega et al. (2014).

Periodic differential reflectivity Z_{dr} calibration is performed using vertical pointing observations (elevation of 90°) made through a full azimuth rotation and colloquially referred to as a "birdbath" scan. Birdbath calibrations are ideally performed when light rain is present over the radar. The full rotation during vertical pointing is necessary to nullify contribution of antenna side-lobe contamination from nearby ground clutter (Bringi and Chandrasekar 2001). Using this method, Z_{dr} calibration of less than 0.2 dB can be attained. An example Z_{dr} calibration scan performed at 0015 UTC 9 June 2013 is shown in Fig. 4. The melting layer can easily be identified in Fig. 4 by the simultaneous increase in reflectivity and decrease in copolar correlation for both Ku- and Ka-band observations. Range volume cells below the melting layer, containing Z_{dr} observations of rain, are averaged over the full rotation and, if necessary, a bias is applied so $Z_{dr} = 0$ dB. The bias is then saved and used for subsequent estimates of Z_{dr}. The Z_{dr} results of rain in Fig. 4 show a near-zero bias in Z_{dr} that requires no adjustment.

Finally, a ray-by-ray calibration (a ray is a full integration period of N pulses) is performed using an internal calibration loop (Vega et al. 2014). This calibration loop provides a means to measure the transmitted power through the receiver path. Using the measurement of transmitted power, variations in the transmitted power and receiver gain can be corrected in the radar equation. Using the internal calibration, both Z_h and Z_{dr} can be corrected for transmitter power drift and receiver gain drift to maintain the accuracy demonstrated by both birdbath scans and sphere calibration.

Using this tiered calibration approach, the D3R system's accuracy is maintained continuously during operation. The sphere calibration results show very

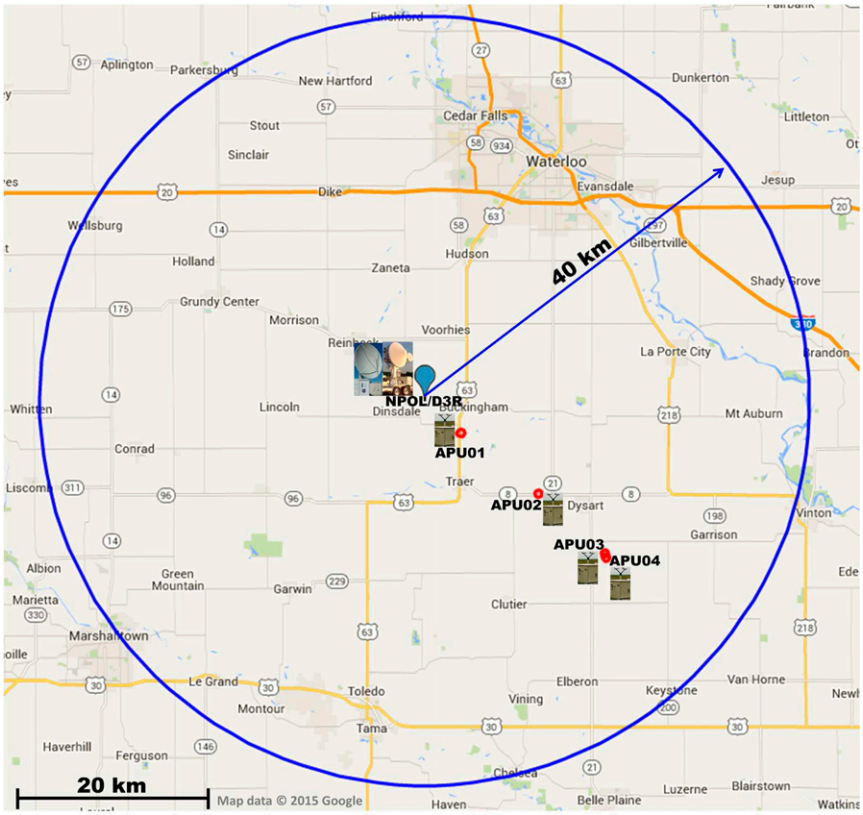

FIG. 1. This map shows the locations of a subset of instruments deployed during the IFloodS field campaign during May and June 2013 located in eastern Iowa. The location of NPOL and D3R is shown with the blue marker. The blue circle with a 40-km radius represents D3R's max observational range. The red dots mark the locations of four disdrometers deployed within D3R's domain.

good calibration of both the Ku- and Ka-band subsystems. Later discussions will compare meteorological estimates with other ground instruments in the IFloodS campaign to further substantiate the calibration quality of the D3R.

b. *Attenuation correction*

The attenuation correction of reflectivity and differential reflectivity observations is a challenging task in weather radars. However, dual-polarization-based attenuation-correction methods have been fairly successful and used widely in the recent years. Many operational systems have implemented differential phase–based attenuation correction (Bringi and Chandrasekar 2001). This can be further improved by more sophisticated attenuation-correction techniques such as the self-consistency approach from Gorgucci and Baldini (2007). The fundamental premise of this attenuation-correction technique is that horizontal and vertical polarization specific attenuation—A_h and A_v, respectively—can be estimated from specific differential phase for frequencies up to Ku band (Bringi and Chandrasekar 2001). We have introduced a preliminary attenuation correction for D3R observations at

TABLE 2. Instrument locations within D3R's observation domain. The range and bearings relative to D3R and NPOL are calculated using the World Geodetic System 1984 Earth model. APU01–APU04 are Autonomous Parsivel Unit disdrometers. SN25, SN35, and SN36 are 2DVDs. The gauges are tipping-bucket rain gauges.

	Lat	Lon	D3R's azimuth	D3R's range (km)
D3R, NPOL	42°16′5.28″N	92°30′34.11″W	—	—
APU01, SN25	42°14′19.54″N	92°27′49.33″W	130.80°	4.99
APU02, SN35, gauge	42°10′56.33″N	92°21′55.55″W	128.67°	15.24
APU03, SN36	42°7′33.52″N	92°16′54.17″W	129.93°	24.56
APU04, gauge	42°7′20.75″N	92°16′50.32″W	130.50°	24.88

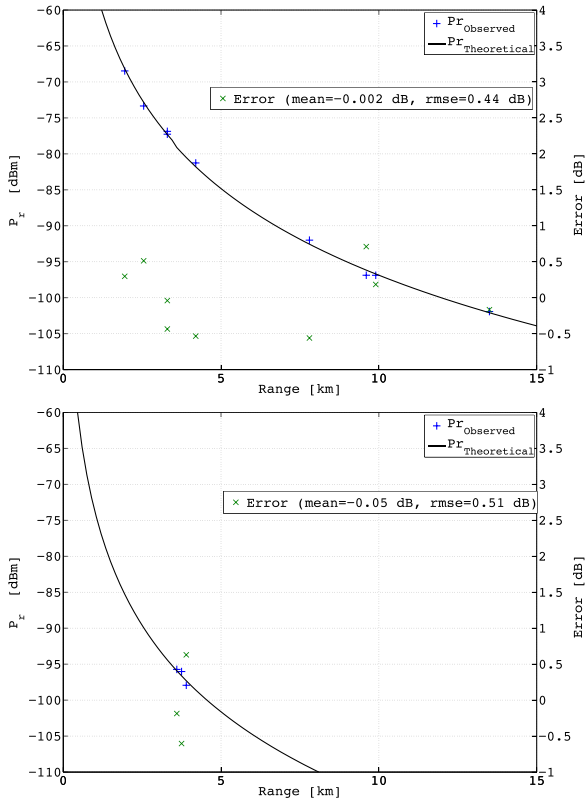

FIG. 2. D3R (top) Ku- and (bottom) Ka-band sphere calibration results from a metal sphere flight beginning at 0000 UTC 14 Jun 2013. The Ku-band results show a Z_h calibration mean error of −0.002 dB with a std dev of 0.44 dB. For the Ka band, the Z_h calibration mean error is −0.05 dB with a std dev of 0.51 dB. Ku- and Ka-band results show excellent reflectivity calibration.

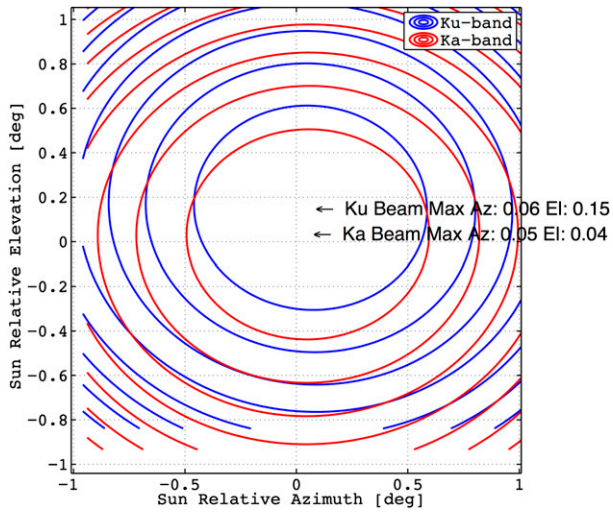

FIG. 3. The D3R antenna coalignment and positioner error verification results at 2247 UTC 18 May 2013. Coalignment of the antennas is within 0.01° in azimuth and 0.11° in elevation. The absolute position error is within 0.06° in azimuth and 0.15° in elevation.

the Ku and Ka bands. A full analysis of attenuation correction is beyond the scope of this paper.

The drop size distributions (DSDs) observed by the four APUs deployed within D3R's domain (see Fig. 1) are used to derive the theoretical relationship among K_{dp}, A_h, and A_v. The APU is an optical disdrometer based on single-particle extinction that measures both particle size and fall velocity (Tokay et al. 2014). Given the DSD data, assumed water temperature of 10°C, and drop shape ratio from Thurai et al. (2007), the dual-polarization radar measurements are simulated using scattering calculations (Waterman 1965). The simulated radar observations include K_{dp} and specific attenuation for each polarization (i.e., A_h and A_v). During IFloodS, the APU temporal sampling resolution was configured for 1-min intervals. In this study, the DSD dataset from the APUs is divided into training and testing datasets. The training dataset is used to estimate a linear relationship between specific attenuation and specific differential phase. The training dataset includes 15 219 (1-min averaged) DSDs collected over nine precipitation days of the IFloodS campaign. The testing dataset, which is independent from the training dataset, is used to verify the accuracy of the model and includes 8631 (1-min averaged) DSDs. Linear regression is applied to the training dataset's specific attenuation and K_{dp} to estimate the model's coefficient (see Figs. 5a,b). The resulting relationship for the Ku-band horizontal polarization specific attenuation $A_h^{(Ku)}$ is

$$A_h^{(Ku)} = 0.4675 K_{dp}^{(Ku)}, \tag{1}$$

and similarly, the Ku-band vertical polarization specific attenuation $A_v^{(Ku)}$ is estimated by

$$A_v^{(Ku)} = 0.3658 K_{dp}^{(Ku)}, \tag{2}$$

where K_{dp} is in degrees per kilometer and the specific attenuation is in decibels per kilometer.

The testing dataset is used to evaluate the model error. The simulated specific attenuation is compared to the model's estimated specific attenuation [Eqs. (1) and (2)] from the simulated K_{dp}. Figures 5c and 5d show scattergrams of the model's estimated specific attenuation versus the intrinsic specific attenuation from simulation. To quantitatively evaluate the accuracy of Eqs. (1) and (2), the mean absolute percentage error (MAPE) is used, defined as

$$\mathrm{MAPE}_{\mathrm{coeff}} = \left\langle \left| \frac{\hat{A} - A}{A} \right| \right\rangle, \tag{3}$$

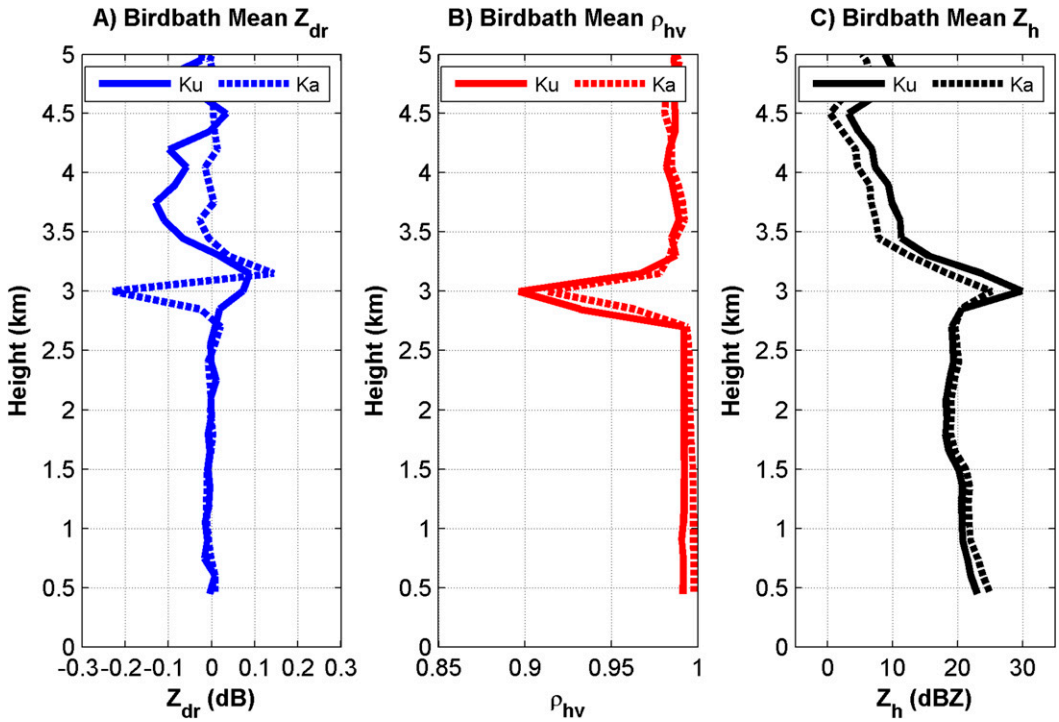

FIG. 4. Calibration results of Z_{dr} from a birdbath scan performed at 0015 UTC 9 Jun 2013 in light stratiform rain. The radar parameters are averaged over a full azimuth rotation. The melting layer is identified by the drop in copolar correlation coincident with an increase in reflectivity at ~3 km. The Z_{dr} for distances below the melting layer, representing rain observations, are adjusted to be 0 dB. From the results, the Z_{dr} bias is ~0 dB for Ku and Ka bands.

where $\hat{A}$ is the K_{dp}-based estimate of specific attenuation, A is the attenuation directly simulated from testing DSD data, and angle brackets denote the sample average. The resulting MAPE values for Eqs. (1) and (2) are 13.7% and 24.8%, respectively.

With the specific attenuation, the path-integrated attenuation (PIA) for the horizontal polarization is calculated by

$$\mathrm{PIA_h}(r) = 2\int_0^r A_\mathrm{h}(s)\,ds \tag{4}$$

and the vertical polarization PIA is similarly calculated as

$$\mathrm{PIA_v}(r) = 2\int_0^r A_\mathrm{v}(s)\,ds, \tag{5}$$

where r is range, s is the propagation interval path length, and both $\mathrm{PIA_h}(r)$ and $\mathrm{PIA_v}(r)$ are in decibels. The attenuation-corrected horizontal reflectivity $\hat{Z}_\mathrm{h}$ is estimated by

$$\hat{Z}_\mathrm{h} = Z_\mathrm{h} + \mathrm{PIA_h}, \tag{6}$$

and the attenuation-corrected differential reflectivity $\hat{Z}_\mathrm{dr}$ is estimated by

$$\hat{Z}_\mathrm{dr} = Z_\mathrm{dr} + \mathrm{PIA_h} - \mathrm{PIA_v}. \tag{7}$$

The K_{dp}-based attenuation-correction methods assume Rayleigh scattering. Attenuation correction of Z_{dr} is subject to overestimation because of deviation from the Rayleigh scattering assumption. The effects of Mie scattering reduce the accuracy of the attenuation correction for Z_{dr} for regions of heavy rainfall. Mie scattering effects can result in a deviation of the actual backscatter and signal extinction cross sections from those predicted from the simple regressions in Eqs. (1) and (2). Similarly, the differential copolar backscatter phase shift δ_{co} cannot be neglected for bigger raindrops. The δ_{co} bias leads to a local overestimation of K_{dp} from the radar's observations of differential phase ψ_{dp} ($\psi_{dp} = \phi_{dp} + \delta_{co}$; where ϕ_{dp} is the propagation differential phase).

For observation volumes with hydrometeors in the Mie scattering regime, the specific attenuation estimates are subject to bias. For Ku-band observations of convective precipitation with intrinsic reflectivity on the order of 45 dBZ or more, the estimation accuracy of specific attenuation may be reduced. For PIA estimation, the bias may not be significant given the overall natural distribution of reflectivity and expected reflectivity estimation accuracy (typically

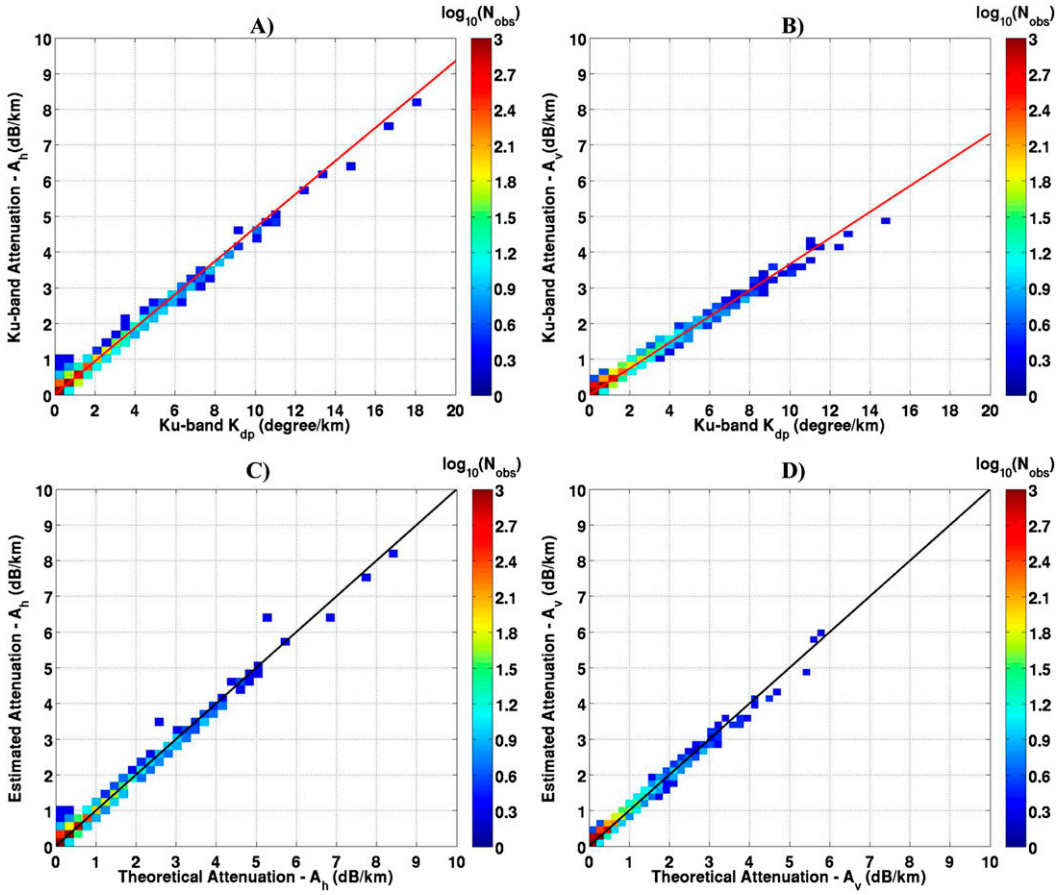

FIG. 5. Simulation results at Ku band using APU-observed DSDs show the relationship between Ku-band specific attenuation and K_{dp}: (a) A_h vs K_{dp} (with a linear fit: $A_h = 0.4675K_{dp}$) and (b) A_v vs K_{dp} (with a linear fit: $A_v = 0.3658K_{dp}$). (c),(d) Scattergrams of attenuations estimated using relations in Eqs. (1) and (2) vs attenuations directly computed using the testing DSD dataset, respectively.

1 dB). For differential PIA, this bias can exceed the expected accuracy for estimates of Z_{dr} (typically 0.2 dB).

The dual-frequency radar configuration is designed to allow a broader class of precipitation to be observed. The Ka-band is intended for light rain and ice microphysical investigation, as attenuation effects are significant for moderate and heavy precipitation. Because of Mie scattering, the simple K_{dp}-based attenuation-correction method does not extend to Ka-band observations for rain. However, the specific attenuations at Ku- and Ka-bands are tightly connected. In this paper, the Ku-band K_{dp} is used to obtain an estimate of Ka-band specific attenuation. Figure 6a shows a scattergram of Ka- versus Ku-band specific attenuation from simulations of the training DSD dataset. For simplicity, the approximated Ka-band specific attenuation is a linearly scaled Ku-band specific attenuation given by

$$A_h^{(Ka)} = 5.8A_h^{(Ku)}. \tag{8}$$

Similarly, we use the testing DSD dataset to evaluate the accuracy of the coefficient in Eq. (8). Figure 6b shows a scatterplot of the Ka-band specific attenuation estimate from Eq. (8) versus the intrinsic Ka-band specific attenuation simulation from the testing DSD data. Evaluating the testing dataset using Eq. (8) yields an MAPE of 41.1% for Ku-band K_{dp} less than $4°\,km^{-1}$. This relationship is determined to be more accurate for the regions where specific attenuation is small; this indicates its viability for use in light and stratiform rain observations during the IFloodS campaign.

The attenuation-correction relationships derived here applied to the D3R observations. These results are compared to other instruments in the IFloodS domain in section 4. The relations in Eqs. (1), (2), and (8) are

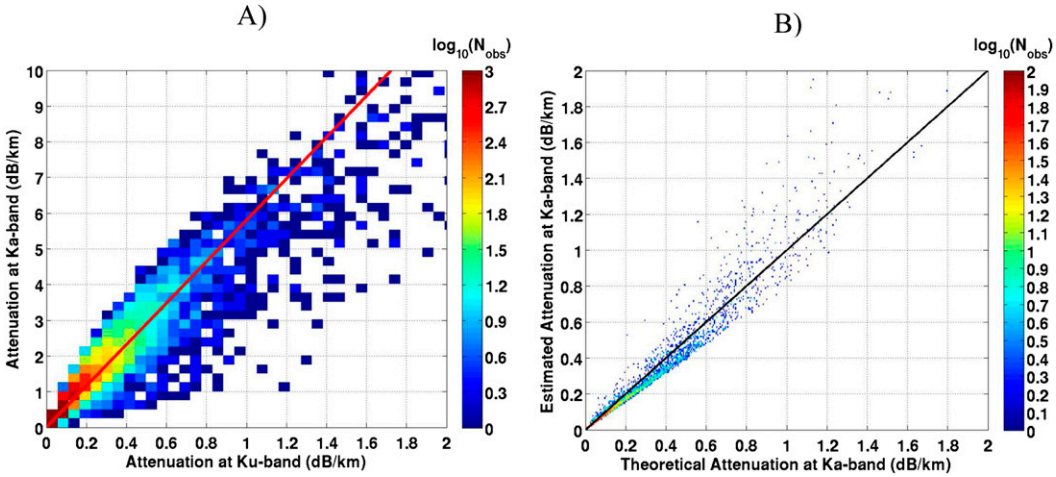

FIG. 6. (a) Scattergram of Ka- vs Ku-band attenuations based on simulations using training DSD dataset. (b) Scattergram of estimated attenuation using Eq. (8) vs theoretical attenuation at Ka band using the testing DSD dataset.

derived particularly for application to observations during the NASA IFloodS field experiment.

4. D3R cross validation with other instruments

The IFloodS field campaign presents a unique opportunity for multi-instrument comparison and cross validation of observations. By comparing observations of precipitation at multiple frequencies, and using ground observations from APU disdrometers, the integrity of the D3R observations will be further established. The microphysical features can also be evaluated in greater detail. As part of the cross validation, both Ku- and Ka-band observations will be compared, and NPOL observations will be considered. In addition, the APU-observed DSDs are used to simulate radar observations at the appropriate frequencies, which are then compared with real radar measurements.

a. Self-consistent attenuation correction and system calibration validation

A self-consistent validation of the radar parameters illustrates that the attenuation correction improves the D3R observations (Scarchilli et al. 1996). The self-consistent relation between reflectivity and differential reflectivity is examined for the D3R Ku-band and NPOL observations. The radar observations are compared to the intrinsic relationship expected using simulated radar parameters from APU-observed DSDs from the field campaign. The self-consistency comparison in Fig. 7 shows the two-dimensional distribution of Z_h versus Z_{dr}; the DSD-based, simulated radar moments are shown as black markers and the attenuation-corrected radar observations (at 1.4° elevation angle) are presented as a two-dimensional color density histogram. The radar observation and simulated results are in good agreement in the distribution range, providing validation that the results, after attenuation correction, are microphysically consistent.

b. Comparison of D3R Ku band and NPOL

The dual-polarization radar observations of the D3R Ku band and NPOL are compared using a plan position indicator (PPI) scan for 1.4° elevation at 2248 UTC 29 May 2013. The results are presented in Fig. 8. The figure compares a D3R Ku band and an NPOL PPI scan of heavy convection embedded in stratiform rain observed at the same elevation and same time. Four radar measurements are considered: Z_h, Z_{dr}, ϕ_{dp}, and copolar correlation ρ_{hv}. Attenuation correction is applied to the observations of reflectivity and differential reflectivity presented here.

A threshold of $\rho_{hv} > 0.80$ is used as a data filter to select observations of precipitation with sufficient signal-to-noise ratio (SNR). From inspection of Fig. 8, the NPOL and the D3R Ku-band results show good agreement in reflectivity. Differential reflectivity agrees well for areas of light and moderate precipitation. The D3R Ku-band Z_{dr} observations are higher than expected along radials for ranges after propagation through areas of intense precipitation. This is because of overcompensation for differential attenuation by the linear attenuation-correction model that is not adequate for correction of Z_{dr} in heavy precipitation at Ku band. The effects of heavy precipitation are evident in the differential phase observations and appear as a large gradient. For areas along the southeastern line of convection, observations have a reduced SNR because of

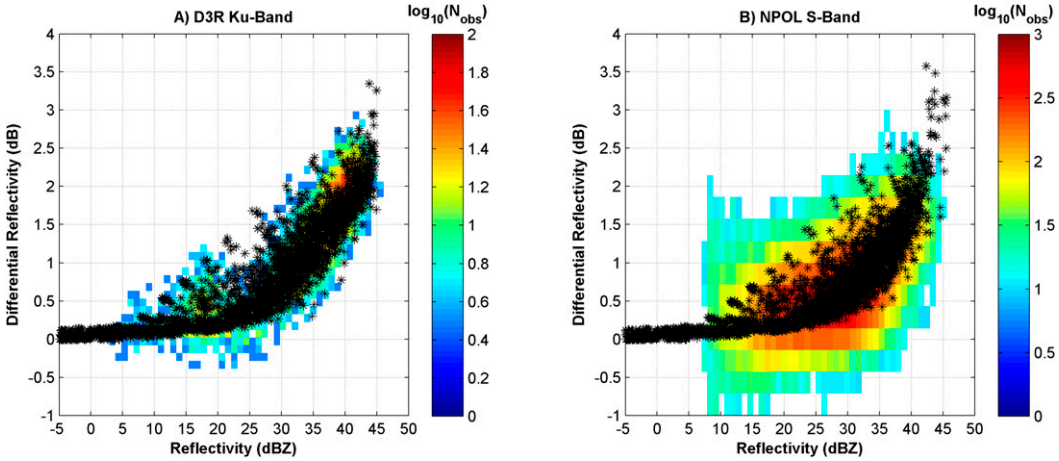

FIG. 7. (a) A histogram showing Z_{dr} vs Z_h of D3R Ku-band observations at 0250 UTC 25 May 2013, after attenuation correction, shown as a color map with Ku-band-simulated results using APU-observed DSDs as black markers. (b) From the same observation time, a histogram of the NPOL observations shown as a color map with S-band-simulated results using APU-observed DSDs as black markers.

signal attenuation. The effect of signal attenuation is evident by decreased ρ_{hv} and high gradient in ϕ_{dp}. The D3R observations in the extreme southeast do not contain data because of signal extinction caused by the line of heavy precipitation.

A detailed ray profile comparison of the observed D3R Ku-band and NPOL reflectivities is shown in Fig. 9. The figure shows a ray plot comparison between the two radars after attenuation correction. Figure 9 also shows simulated S-band observations using the APUs in D3R's observation domain. The radial selected is at azimuth 128.4°, which is in line with the APU disdrometers and at an elevation of 1.4°. The S-band simulated reflectivity, using DSD observations from APU02, APU03, and APU04 at the same time period, are shown as black markers in Fig. 9. The two radars and three APUs show excellent agreement in the reflectivity estimates. For this observation, the root-mean-square error (RMSE) between the D3R and NPOL observations is 2.8 dB for ranges after 13 km with observations having a copolar correlation greater than 0.9.

c. *Dual-frequency ratio*

Dual-frequency ratio (DFR) is the ratio of reflectivities at two radar frequencies. Dual-frequency ratio is an important observed parameter that aids in describing the microphysical characteristics of the radar volume. For the GPM DPR, DFR is an important parameter used in algorithms for microphysical retrieval and hydrometeor classification. The D3R design inherently provides temporal and spatial synchronization between the Ku and Ka bands. The simultaneous, aligned observations allow for direct calculation of DFR. The measured dual-frequency ratio (DFR_m) is the difference between the observed reflectivity at two frequencies without attenuation correction; DFR_m and DFR differ only in attenuation correction. For the D3R,

$$\mathrm{DFR}_m = Z_h^{(\mathrm{Ku})} - Z_h^{(\mathrm{Ka})}. \tag{9}$$

The D3R Ku- and Ka-band observations of a convective cell with stratiform and ice aloft is shown in Fig. 10. The convective cell was observed at 0405 UTC 21 May 2013, and the Ku-band reflectivity, Ka-band reflectivity, and DFR_m are shown in Fig. 10. It should be noted that no attenuation correction has been applied to the observations presented, and only data with $\rho_{hv} > 0.8$ are shown as a means to filter low SNR observations. In this case, attenuation due to precipitation does not significantly impact reflectivity observations for ranges near the radar where only light precipitation ($Z_h < 10\,\mathrm{dB}Z$) is observed. Similarly, regions of ice do not have significant attenuation effects, as attenuation from ice is less pronounced than attenuation from water particles.

From the DFR_m observation in Fig. 10, two radial reflectivity profiles are presented in Fig. 11. The observations have been averaged for longer duration (576 ms vs 64 ms in Fig. 10) to reduce the effects of measurement fluctuations. The presented reflectivity observations are echoes from ice crystals in the observed convective cell in Fig. 10. Figures 11a and 11c consider a radial covering 15.1°–16.2° for reflectivity and DFR, respectively. Figures 11b and 11d consider a radial covering 30.1°–31.1° for reflectivity and DFR_m,

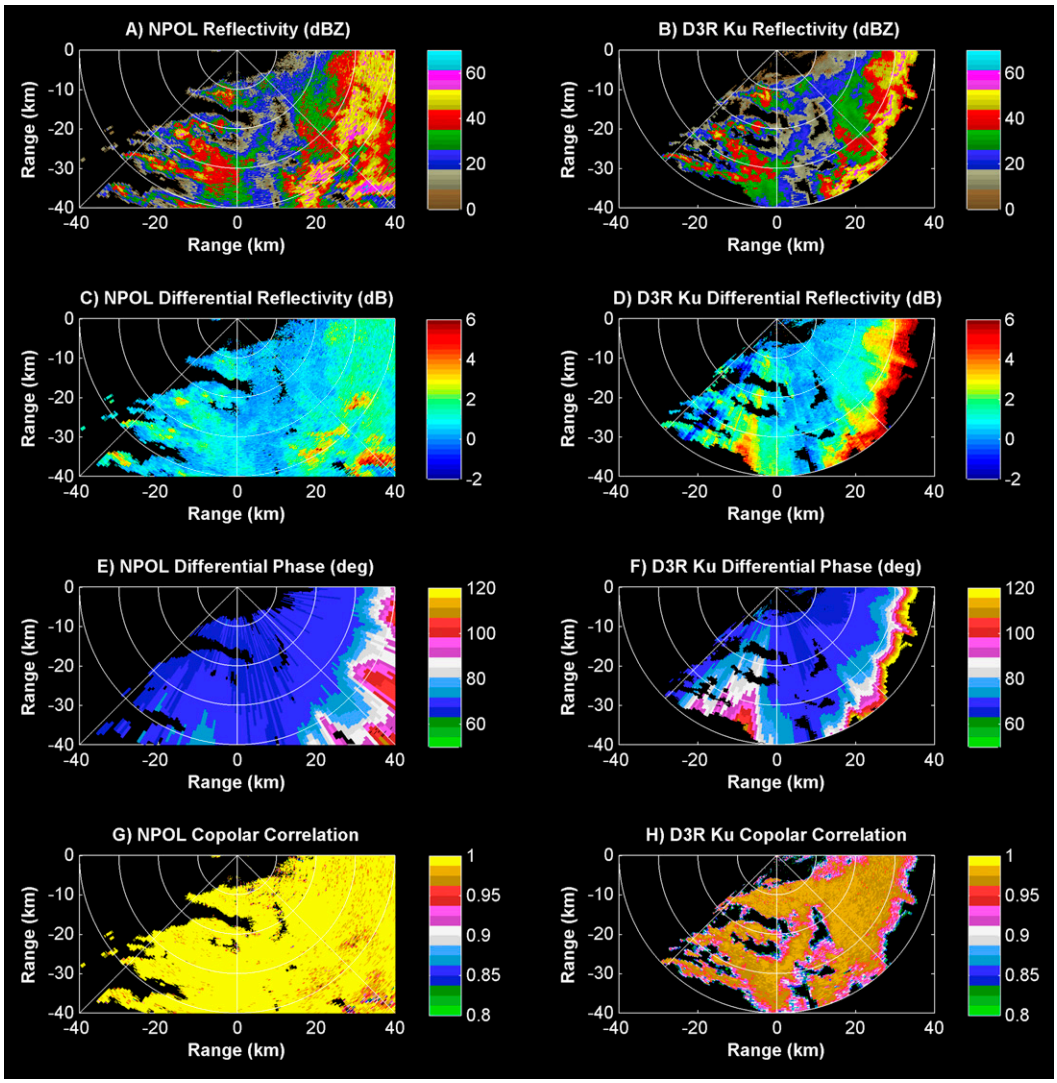

FIG. 8. Radar observations from PPI scans for 1.4° elevation at 2248 UTC 29 May 2013. (left) NPOL observations after attenuation correction. (right) D3R Ku-band attenuation-corrected observations. Note that the extinction of the D3R Ku-band signal results in a mismatch of observations in the southeastern quadrant. The NPOL range extends to 100 km while D3R range limit is 39.75 km.

respectively. The two different elevations observe different projections of the echo's polarimetric signature onto the radar as well as different ice crystal densities. The observed DFR_m values in Figs. 11c and 11d are consistent with the reported simulation values of DFR for Ku- minus Ka-band reflectivity observations of ice crystal aggregates (Tyynelä and Chandrasekar 2014).

Next, the dual-frequency ratio of rain will be considered from an RHI observation of stratiform rain at 1530 UTC 27 May 2013. The attenuation-corrected reflectivity profiles at Ku and Ka bands are presented in Figs. 12a and 12b, respectively. Examination of the reflectivity plots shows signal extinction as a result of signal attenuation in rain, which is apparent in the Ka-band observations when compared to the Ku-band results.

Figure 13 presents simulations of radar observations using APU-observed DSDs at 0° in elevation. The effects of Mie scattering result in a nonlinear relationship between Ku- and Ka-band reflectivity. The nonlinear behavior is characterized in greater detail by the dual-frequency ratio versus Ku-band reflectivity in Fig. 13 (middle). The median raindrop equivalent volume diameter D_0 is defined such that drops less than D_0 contribute to half the total rainwater content W (Bringi and Chandrasekar 2001) and can be estimated from the following relationships:

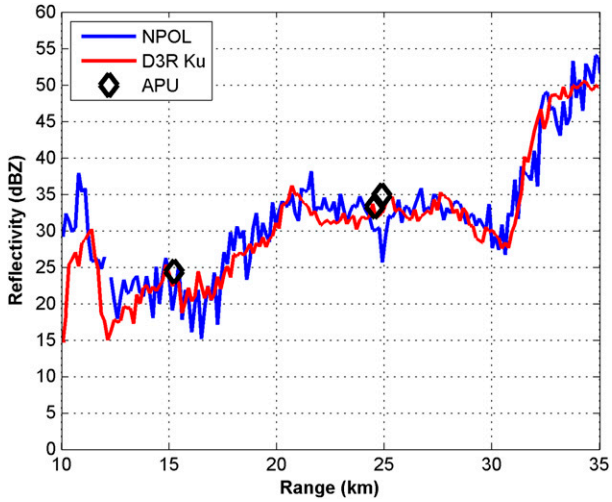

FIG. 9. Comparison of the D3R Ku-band, NPOL, and S-band simulated reflectivity using APU-observed DSDs. All observations are at 2248 UTC 29 May 2013. The presented NPOL and D3R reflectivity are from the same radial. Note that signal extinction results in a mismatch between NPOL and D3R, followed by a loss of data after approximately the 35-km range.

$$\frac{\pi}{6}\rho_w \int_0^{D_0} D^3 N(D)\, dD = \frac{1}{2}\frac{\pi}{6}\rho_w \int_0^{\infty} D^3 N(D)\, dD = \frac{1}{2}(W), \tag{10}$$

where D is the raindrop equivolume diameter and ρ_w is the density of water. With the relationship in Fig. 13 (right), D_0 can be estimated directly from DFR observations (Meneghini et al. 1997).

From observations presented in Fig. 12, a direct comparison of the D3R's estimated reflectivities along an aligned radial is shown in Fig. 14. The radial is at approximately 1.5° in elevation with an integration period of 320 ms. Observations from 5 to 16 km in range showed good agreement between Ku- and Ka-band reflectivity estimates. At 15 km, simulated Ku-band reflectivity from APU02-observed DSDs is presented and is also in good agreement with observed reflectivities. Using the results of Fig. 13 (right) and the DFR estimates of Fig. 14b, the D_0 for the stratiform rain observations along the radial are between 1.3 and 2.0 mm, which is consistent with the estimate of D_0 from the APU02 disdrometer of 0.954 mm for the observation period.

5. Ku-band QPE

The D3R Ku-band provides an effective means to quantitatively estimate precipitation rate and total rainfall accumulation, especially in light rain. It has been shown that various rainfall algorithms can be derived

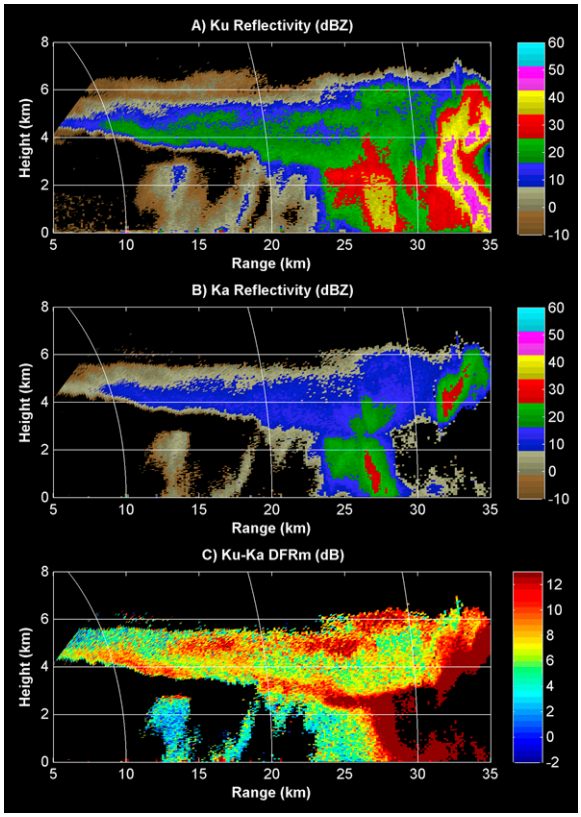

FIG. 10. RHI observations at 0405 UTC 21 May 2013 of a convective cell with lofted ice. No attenuation correction has been applied and data with a copolar correlation coefficient greater than 0.8 are shown. The measured (a) Ku- and (b) Ka-band reflectivity is shown. (c) The D3R DFR_m (Ku minus Ka band) results. The DFR_m values at or above 13 dB are shown as the 13-dB value.

with respect to dual-polarization radar measurements via the DSD information (Bringi and Chandrasekar 2001). However, the choice of rainfall relations at Ku band gets complicated since Z_h and Z_{dr} must be corrected for attenuation before being used for rainfall estimation. Therefore, we consider only $R(K_{dp})$ for rainfall estimation with the D3R. At Ku band, $R(K_{dp})$ is the only estimator not affected by signal attenuation due to propagation through precipitation. In addition, $R(K_{dp})$ is not sensitive to hail contamination or absolute calibration errors of the radar system (Bringi and Chandrasekar 2001).

A Ku-band $R(K_{dp})$ relation is developed based on disdrometer observations collected during the IFloodS field experiment in Chen and Chandrasekar (2015). The $R(K_{dp})$ relationship is given by

$$R = 10.43 K_{dp}^{0.88}. \tag{11}$$

The rainfall rate R is measured in millimeters per hour and K_{dp} has units of degrees per kilometer. As with the

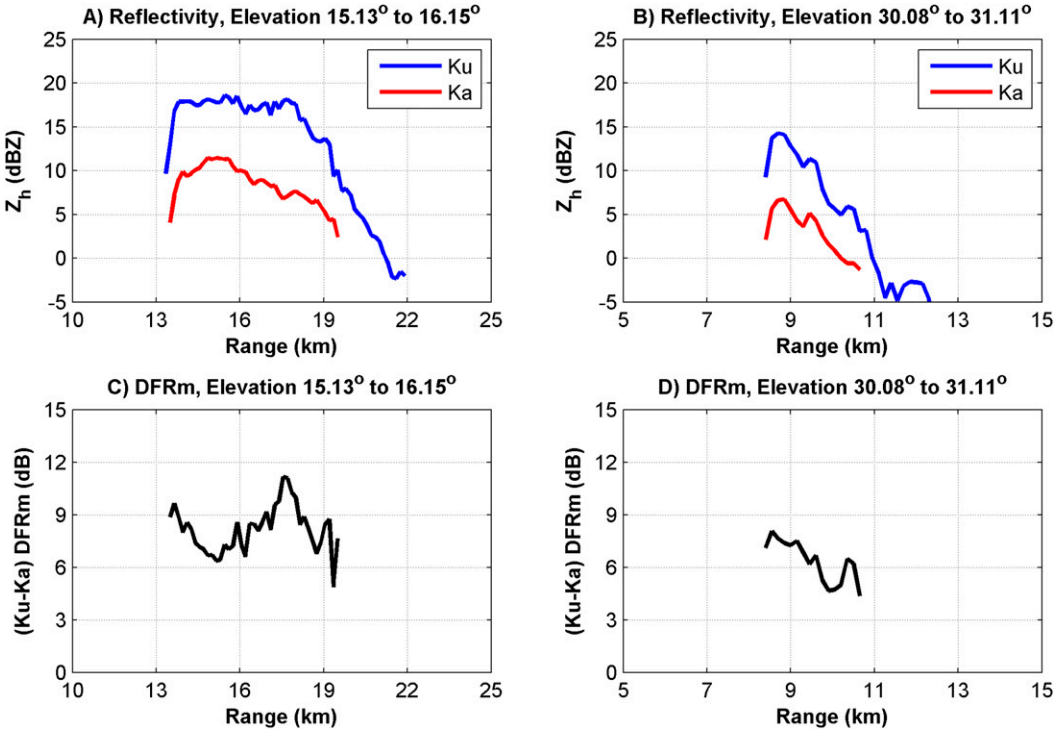

FIG. 11. Two radials representing the observations of lofted ice in Fig. 10. The (a),(b) observed Ku- and Ka-band reflectivity (without attenuation correction) and (c),(d) difference between the reflectivities (shown as DFR_m). The observed DFR_m is consistent with simulations of DFR for aggregates of ice crystals (Tyynelä and Chandrasekar 2014). The radials are integrated over 576 ms (1152 pulses) to estimate reflectivity and only observations with $\rho_{\mathrm{hv}} > 0.8$ are shown.

estimation of specific attenuation, the methodology proposed in Wang and Chandrasekar (2009) is implemented for the D3R to estimate K_{dp}.

Using Eq. (11), the rainfall rate is estimated every 1 min based on the scanning strategy for the D3R. To evaluate the performance of the D3R rainfall product, 5-min rainfall observations from ground instruments are used as a reference for cross comparison. The ground instruments considered are two pairs of collocated APUs and tipping-bucket rainfall gauges. For

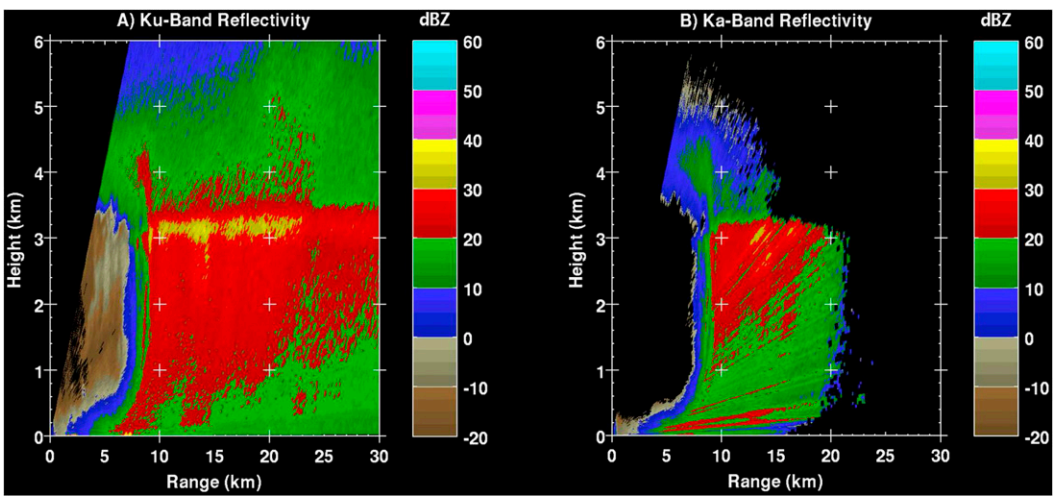

FIG. 12. Reflectivity observations at 1530 UTC 27 May 2013 of an RHI scan through stratiform rain for (a) Ku and (b) Ka band after attenuation correction.

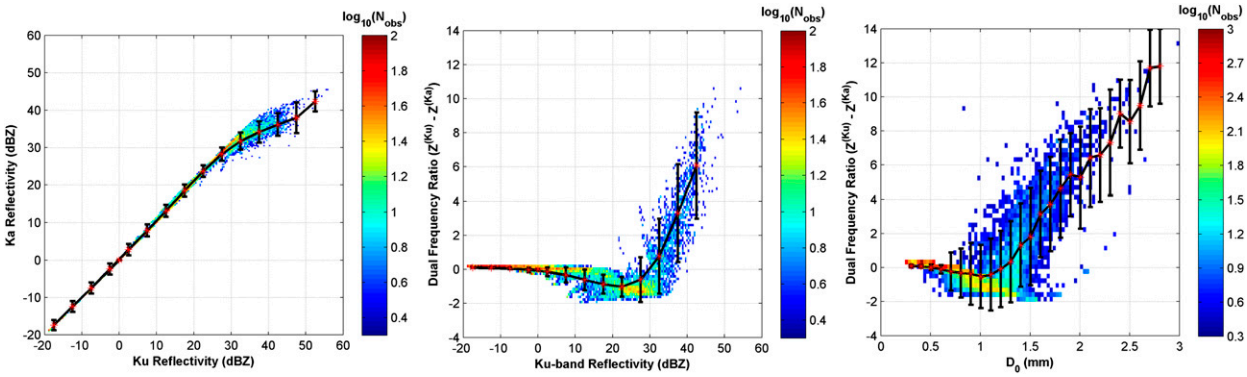

FIG. 13. The intrinsic (left) Ka- vs Ku-band reflectivity, (middle) DFR vs Ku-band reflectivity, and (right) DFR vs D_0. All results are from the simulation of APU-observed DSDs. The vertical black lines extend one std dev from the mean. The black line with red markers represents the mean. Histogram values with two or less observations are omitted for clarity but are used for estimates of the mean and errors.

comparison between the instruments, the D3R's rainfall is presented as 5-min rainfall accumulations of the 1-min estimated rainfall rates. To evaluate the D3R QPE performance in a quantitative manner, the normalized standard error (NSE) is defined as

$$\mathrm{NSE}_R = \frac{\langle |R_r - R_a| \rangle}{\langle |R_a| \rangle}, \tag{12}$$

where R_r is the radar estimate of rainfall, R_a is the APU measurement of rainfall, and angle brackets denote averaging over the observation time period.

Figure 15 compares the 5-min rainfall accumulation observations on 28 May 2015. The D3R Ku-band estimates at two locations during the same time period are considered: the location of the APU02 and APU04 disdrometers. The observation period on 28 May 2013 is of a widespread stratiform event. It can be seen from Fig. 15 that the radar measurements agree very well with the observations from the APUs and rain gauge measurements. For the 28 May 2013 sample event shown in Fig. 15, it is concluded that the NSE for the 5-min rainfall accumulations is 36.9%. The NSE statistic is computed based on observations at both the APU02 and APU04 locations.

It should be mentioned that rain gauge observations are not used here for quantitative evaluation because the tipping-bucket gauges suffer from significant errors in light rain cases. The rainfall accumulation resolution of the gauge is 0.254 mm (0.01 in.). For light rain or high temporal sampling, the gauge resolution is not adequate and highlights the limited applicability of rainfall gauge data for use in light to moderate rainfall rates with high-temporal-resolution models. The rain gauge error during light rain at high temporal resolution is evident from review of Fig. 15.

Figure 16 shows example 5-min rainfall comparisons on 29 May 2013, characterizing a strong convective storm. It can be seen from Fig. 16 that the radar measurements agree with the observations from the APUs and rain gauge measurements very well for this convective case. The NSE for the 5-min rainfall accumulation is 49.4% using observations from both APU02 and APU04. Similarly, the NSE between radar rainfall accumulations and rain gauge measurements (collocated

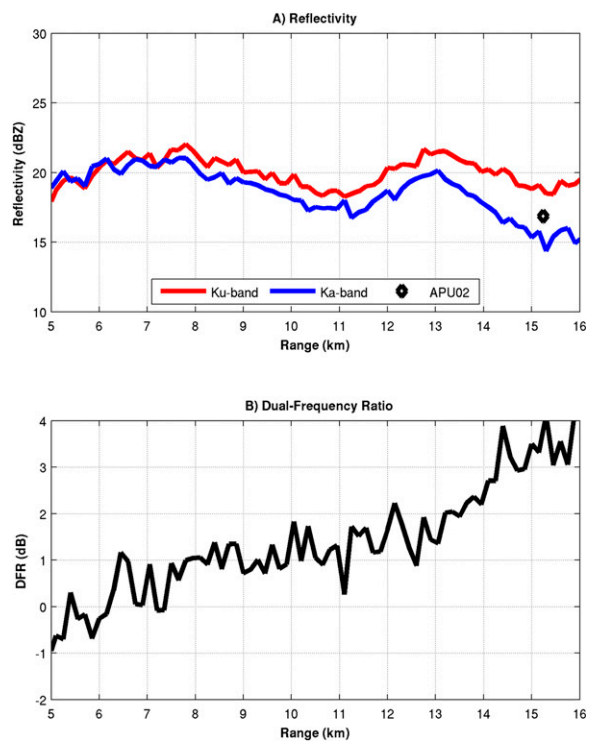

FIG. 14. (a) Ku- and Ka-band reflectivity along a radial covering 1.0°–1.5° elevation from Fig. 12. Five consecutive rays were averaged to produce the results. (b) The DFR (Ku- minus Ka-band reflectivity) for the same observations.

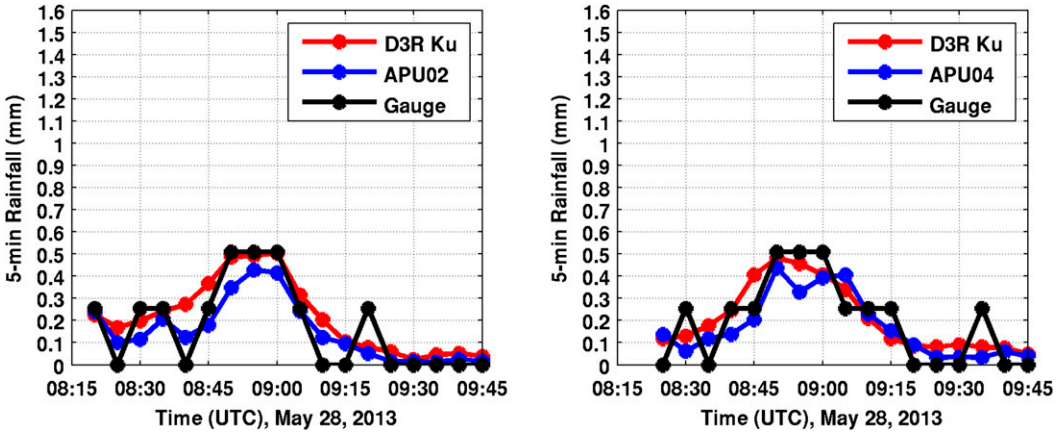

FIG. 15. The 5-min rainfall accumulation estimates from 28 May 2013 using D3R Ku-band, APU02 and APU04 disdrometers, and rain gauge collocated with disdrometers. The observations are of widespread stratiform rain.

with APUs) is computed for this convective case as 45.6%.

The quantitative precipitation estimation results demonstrate D3R as an excellent platform for rain-rate estimation in light rain mainly because of the increased sensitivity of K_{dp} at Ku band over lower frequencies such as S band. The high-temporal-resolution QPE results presented demonstrate the capability of Ku-band observations for monitoring fast-moving precipitation with a high degree of accuracy.

6. Summary

The D3R was deployed as part of a focused multi-instrument ground validation field experiment to support the GPM program. D3R is a well-calibrated, accurate instrument for microphysical investigation of meteorological phenomena. The collocated D3R and NPOL enabled coordinated multifrequency observations of precipitation at fine spatial and temporal resolution. The coordinated observations in IFloodS extend across multiple, diverse, and densely deployed ground instruments for in situ microphysical observations and measurement of rain rates. This experiment provided the conclusive end-to-end system validation for the D3R as a deployable radar system.

The D3R's various methods of calibration and verification were presented for the IFloodS field campaign. All results show the D3R system operates in a state with excellent calibration, which was confirmed by self-consistent validation derived from microphysical relationships and comparison with a variety of instruments deployed in the D3R's observational domain. Using simulation results from APU disdrometer DSD observations, attenuation-correction relations specific to the region were determined for the D3R. The

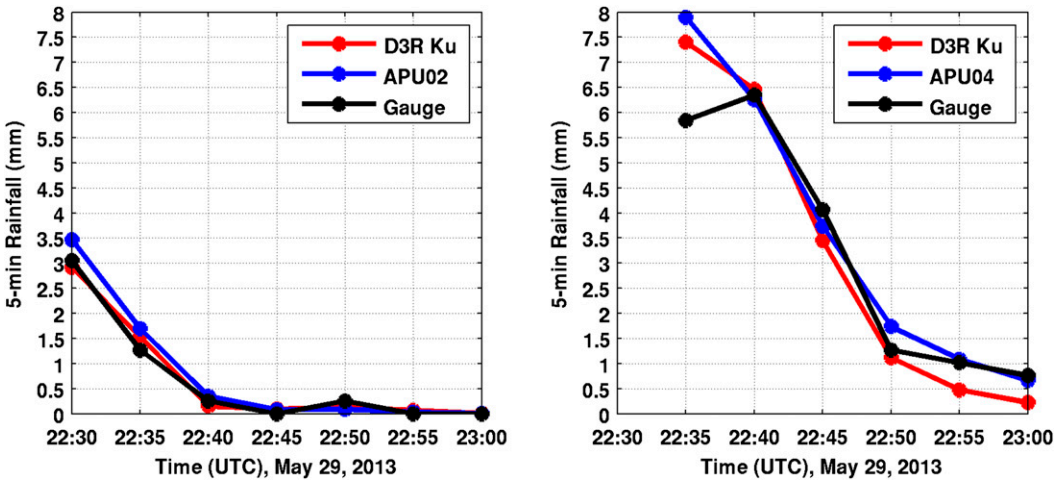

FIG. 16. The 5-min rainfall accumulation estimates from 29 May 2013 using D3R Ku-band, APU02 and APU04 disdrometers, and rain gauge collocated with disdrometers. The observations are of convective rain.

attenuation-correction performance was similarly verified against other instruments. The D3R shows very good agreement with both ground-based disdrometers as well as the collocated NPOL.

From the D3R observations, examination of the sample microphysical characteristics of the IFloodS domain is presented. Dual-frequency ratio observations of ice and rain were shown for simultaneous Ku- and Ka-band observations. The DFR_m observations of ice were consistent with theoretical values for aggregate ice crystals. The DFR observation in light, stratiform precipitation yielded estimates of the median raindrop diameter and verified using an APU disdrometer's estimate of D_0. Finally, high temporal sampling of rainfall using the Ku-band observations was demonstrated for a stratiform rain case and a convective rain case. The normalized standard error results from the D3R comparison with APUs demonstrate that good performance is attainable using Ku-band observations for light rain observations with high temporal update rates.

Acknowledgments. The authors acknowledge the support of the GPM program, David Wolff and David Marks for NPOL support, and Mathew Schwaller and Walter Petersen for deployment and logistics support. In addition, the authors acknowledge all the participants of the IFloodS field campaign.

REFERENCES

Bringi, V. N., and V. Chandrasekar, 2001: *Polarimetric Doppler Weather Radar: Principles and Applications.* Cambridge University Press, 664 pp.

Chen, H., and V. Chandrasekar, 2015: Estimation of light rainfall using Ku-band dual-polarization radar. *IEEE Trans. Geosci. Remote Sens.*, **53**, 5197–5208, doi:10.1109/TGRS.2015.2419212.

Gorgucci, E., and L. Baldini, 2007: Attenuation and differential attenuation correction of C-band radar observations using a fully self-consistent methodology. *IEEE Geosci. Remote Sens. Lett.*, **4**, 326–330, doi:10.1109/LGRS.2007.894162.

Hillaker, H. J., 2013: Preliminary Iowa weather summary–2013. Iowa Dept. of Agriculture, accessed 2 February 2015. [Available online at www.iowaagriculture.gov/climatology/weatherSummaries/2013/pas2013.pdf.]

Meneghini, R., H. Kumagai, J. R. Wang, T. Iguchi, and T. Kozu, 1997: Microphysical retrievals over stratiform rain using measurements from an airborne dual-wavelength radar-radiometer. *IEEE Trans. Geosci. Remote Sens.*, **35**, 487–506, doi:10.1109/36.581956.

Scarchilli, G., E. Gorgucci, V. Chandrasekar, and A. Dobaie, 1996: Self-consistency of polarization diversity measurement of rainfall. *IEEE Trans. Geosci. Remote Sens.*, **34**, 22–26, doi:10.1109/36.481887.

Thurai, M., G. J. Huang, V. N. Bringi, W. L. Randeu, and M. Schönhuber, 2007: Drop shapes, model comparisons, and calculations of polarimetric radar parameters in rain. *J. Atmos. Oceanic Technol.*, **24**, 1019–1032, doi:10.1175/JTECH2051.1.

Tokay, A., D. B. Wolff, and W. A. Petersen, 2014: Evaluation of the new version of the laser-optical disdrometer, OTT Parsivel^2. *J. Atmos. Oceanic Technol.*, **31**, 1276–1288, doi:10.1175/JTECH-D-13-00174.1.

Tyynelä, J., and V. Chandrasekar, 2014: Characterizing falling snow using multifrequency dual-polarization measurements. *J. Geophys. Res. Atmos.*, **119**, 8268–8283, doi:10.1002/2013JD021369.

Vega, M. A., V. Chandrasekar, J. Carswell, R. M. Beauchamp, M. R. Schwaller, and C. M. Nguyen, 2014: Salient features of the dual-frequency, dual-polarized, Doppler radar for remote sensing of precipitation. *Radio Sci.*, **49**, 1087–1105, doi:10.1002/2014RS005529.

Wang, Y., and V. Chandrasekar, 2009: Algorithm for estimation of the specific differential phase. *J. Atmos. Oceanic Technol.*, **26**, 2565–2578, doi:10.1175/2009JTECHA1358.1.

Waterman, P. C., 1965: Matrix formulation of electromagnetic scattering. *Proc. IEEE*, **53**, 805–812, doi:10.1109/PROC.1965.4058.